Models of Post-Translational Protein Translocation

Timothy C. Elston
Biomathematics Graduate Program/Department of Statistics, North Carolina State University, Raleigh, North Carolina 27695-8203 USA

ABSTRACT Organellar Hsp-70 is required for post-translational translocation into the endoplasmic reticulum and mitochondria. The functional role played by Hsp-70 is unknown. However, two operating principles have been suggested. The power stroke model proposes that Hsp-70 undergoes a conformational change, which pulls the precursor protein through the translocation pore, whereas, in the Brownian ratchet model, the role of Hsp-70 is simply to block backsliding through the pore. A mathematical analysis of both mechanisms is presented and reveals that qualitative differences between the models occur in the behavior of the mean velocity and effective diffusion coefficient as a function of Hsp-70 concentration. An experimental method is proposed for measuring these two quantities that only relies on current experimental techniques.

INTRODUCTION

Many proteins synthesized in the cytosol must be transported across one or two membranes to reach their final destination. In mammalian cells, the only mode of importation into the endoplasmic reticulum (ER) appears to be cotranslational with the ribosome attached directly to the channel. However, post-translational translocation, in which the nascent protein is transported after release from the ribosome, has been observed in yeast. In this paper, only post-translational translocation is considered. Two mechanistic models for this process have been purposed and have been referred to as the "Brownian ratchet" and "translocation motor" (Simon et al., 1992; Glick, 1995). Unfortunately, experimental data does not definitively rule out either model. In this paper, a mathematical analysis of both models is presented. The results of these investigations reveal that the two models make qualitatively different predictions. The differences are observed in the behavior of the mean velocity and effective diffusion coefficient as a function of organellar Hsp-70 concentration. However, direct measurement of these two quantities is not currently possible. Therefore, we propose a method for determining the mean velocity and effective diffusion coefficient that only requires monitoring the fraction of protein released from the translocation channel as a function of time.

Two commonly studied post-translational translocation systems are those found in the ER and mitochondria. In both systems, a signal sequence near the amino terminus targets the precursor protein for import. In the ER, the central channel-forming protein is believed to be Sec-61 (Gorlich and Rapoport, 1993). On the lumenal side of the membrane Sec-61 associates with a Sec-62/63p complex (Panzner et al., 1995). The J domain of Sec-63p interacts with organellar BiP, a member of the Hsp-70 family of ATPases. BiP also binds to the precursor protein and is responsible for providing directionality to the process (Matlack et al., 1999). The mitochondrial envelope consists of two membranes. Initially, both ATP hydrolysis and an electrostatic potential across the inner membrane are used to drive the signal sequence into the mitochondrial matrix. After the signal sequence has entered the matrix, translocation relies on ATP hydrolysis alone (Ungermann et al., 1996; Hwang et al., 1991). In mitochondria, mHsp-70 plays the role of BiP and Tim-44 the role of Sec-63p.

The mechanism that drives post-translational translocation is not known, and two different roles for organellar Hsp-70 have been suggested. In the first scenario, Hsp-70 associates with both the membrane bound complex (Sec-63p or Tim-44) and the precursor protein. Hsp-70 then undergoes an ATP-dependent conformational change that pulls the precursor through the pore (Glick, 1995). In the second scenario, the role of Hsp-70 is simply to prevent backward diffusion of the precursor protein (Schneider et al., 1994; Simon et al., 1992), and import relies on biased thermal diffusion. It should be noted that both models represent "molecular motors" in that chemical-free energy is used to produce directed motion. Therefore, the term translocation motor, which was introduced by Glick (1995) to describe the first scenario, applies to both mechanisms. We adopt the more descriptive term "power stroke model" when referring to the case in which Hsp-70 actively pulls the precursor through the translocation pore and use Brownian ratchet to refer to the case where translocation is driven solely by biased thermal motion.

Data presented in two recently published articles have been used to argue for each model (Matlack et al., 1999; Voisine et al., 1999). Here we restate the arguments provided by the respective authors to support their views. It is left to the interested reader to determine the validity of these arguments by reviewing the papers and references therein. The work of Matlack et al. (1999) has provided evidence that indicates that a Brownian ratchet is sufficient for importing proteins into the ER. This evidence comes from the observation that replacing BiP with antibodies against the precursor still leads to translocation of the precursor, albeit

Received for publication 22 December 1999 and in final form 30 July 2000.
Address reprint requests to Tim Elston, North Carolina State University, Biomath Program, Dept. of Statistics, Box 8203, Raleigh, NC 27695-8203. Tel.: 919-515-1910; Fax: 919-515-1909; E-mail: elston@stat.ncsu.edu.

0006-3495/00/11/2235/17 $2.00

less efficiently than with BiP. This result shows that an interaction with the channel complex and ATP hydrolysis are not required for import into the ER. That is, translocation can be driven by biased thermal diffusion with binding free energy fueling the process. Recent evidence for the power stroke model comes from mutational studies (Voisine et al., 1999). In this work, a mutation in the peptide-binding domain of mitochondrial Hsp-70 that interferes with the protein's ability to interact with Tim-44 was studied. The mutant form of mHsp-70 was unable to import precursors that possess tightly folded domains, but were imported by wild-type mHsp-70. However, less tightly folded proteins were imported by the mutant mHsp-70. Thus, it seems that the mutation affected the force-generating step, but still allowed mHsp-70 to act as a molecular ratchet. Another result from these investigations, which can be interpreted as being at odds with the Brownian ratchet, is that a reduction in ATP concentration produced an increased association of mHsp-70 with the precursor, while at the same time the import efficiency was reduced.

The remainder of the paper is organized as follows. In the next section a description of both models is provided. The chemistry involved in the two models is identical. Where the models differ is the mechanical mechanism used to advance the precursor. For the power stroke model, both a power stroke and biased thermal diffusion drive translocation. The Brownian ratchet represents a limiting case of the power stroke model in which the strength of the power stroke is zero. In the section Mathematical Framework, the models are formulated mathematically. An important aspect of this section is the discussion of three approximations that can be used to construct asymptotic solutions to the model equations. The validity of the approximations requires that the time scale set by thermal diffusion is long, compared to that of the chemical kinetics. This is an appropriate limit in which to study protein translocation, because strong precursor–pore interactions significantly reduce the diffusion coefficient of the precursor. The validity of this claim, which was originally proposed by Chauwin et al. (1998), is addressed in the Discussion section. The approximations are presented in order of increasing accuracy. In the Results, differences between the two models are discussed, and an experimental procedure for measuring the average velocity and effective diffusion coefficient of the precursor is presented. The main body of the manuscript ends with some concluding remarks. In Appendix B, a discussion of the approximate solutions is presented. The approximations are important for two reasons: they provide physical insight into the models and they require less computational time than performing numerical simulations.

DESCRIPTION OF THE MODELS

Figure 1 *A* shows the mechanochemical cycle of the power stroke model that drives translocation. The chemical steps shown in this figure are similar to those postulated by Horst et al. (1997). In the first step, Hsp-70·ATP associates with the channel complex and loosely with the precursor protein. Next Hsp-70 hydrolyzes ATP to produce Hsp70·ADP·Pi, which forms a stable bond with the precursor. In the third step, the release of Pi causes Hsp-70·ADP to undergo a conformational change. The result of this conformational change is that, now, Hsp-70 is under strain when bound to both the precursor and the channel complex. This strain is released by pulling the precursor through the pore. In Fig. 1 *A*, we illustrate the strain as resulting from the release of energy stored in a cocked spring. This is highly schematic and not meant to represent an actual conformational change. We postulate that the release of Hsp-70 from the channel complex is not a rate-limiting step, so that it is possible for multiple binding and release events with the channel to take place during the power stroke phase. If the release of Hsp-70 from the channel does turn out to be a rate-limiting step, then the effectiveness of both models is reduced, because a significant fraction of time is spent in a "stuck" state with precursor unable to advance. The important point is that, until the precursor has moved sufficiently far, Hsp-70 must assume a strained configuration when bound with the precursor and channel complex. The release of this strain results in an effective power stroke. In the fourth step, the power stroke has been completed, and the precursor has moved far enough to allow the next binding site to enter the organelle. The association of a new Hsp-70·ATP with this binding site requires that the Hsp-70·ADP nearest the membrane fluctuate out of the way. In the figure, this has been illustrated by a rotation of the portion of the precursor inside the organelle by 180°. However, in reality, such a large fluctuation would not be required. It is also possible that, for a new Hsp-70·ATP to bind after the completion of the power stroke, the precursor must diffuse forward by some amount. This effect can be included in the model by making the potential that generates the power stroke flat during the diffusive portion of precursor advancement. This will reduce the effective power stroke felt by the precursor, but not change qualitative features of the result presented below. What is not shown in Fig. 1 *A* is the release of ADP (in mitochondria this involves the nucleotide exchange factor mGrpE), and subsequent rebinding of ATP, which is thought to promote the release of Hsp-70 from the precursor. However, these steps are taken into account in the mathematical description through the inclusion of a dissociation rate. The chemical steps shown in Fig. 1 *B* for the Brownian ratchet are identical with those of the Fig. 1 *A*. The only difference between the two models is that, for the Brownian ratchet, the release of Pi does not produce a conformational change in Hsp-70. Therefore, the transition 3→4 shown in Fig. 1 *B* is driven by diffusion alone.

For the remainder of this paper, we make the assumptions that transitions 1→2 and 2→3 are effectively irreversible and that these transitions are not rate limiting. These as-

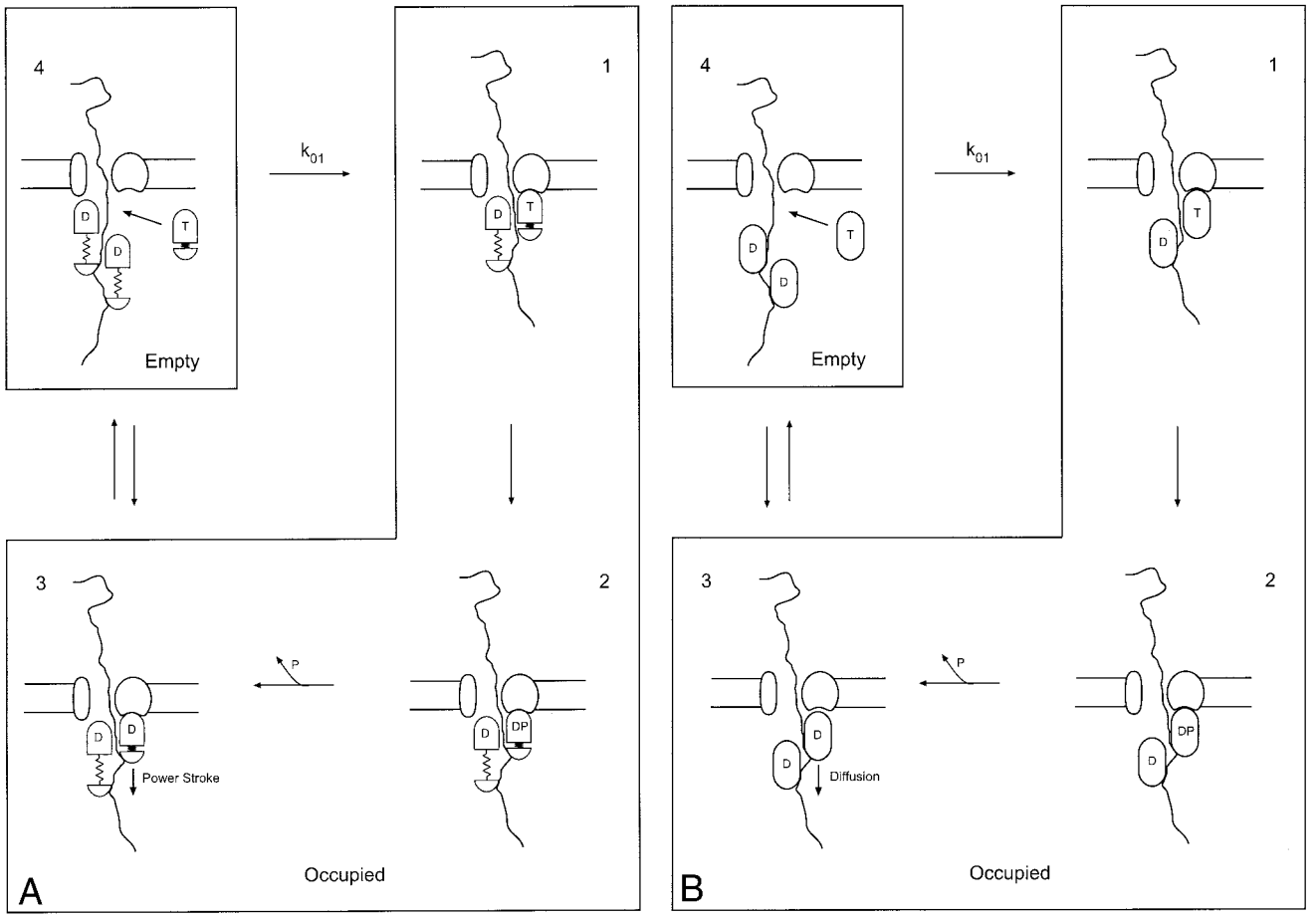

FIGURE 1 (*A*) The mechanochemical cycle of the power stroke model. In chemical state 1 Hsp-70·ATP is bound to the channel complex and associates loosely with the precursor. In transition 1→2, ATP is hydrolyzed. This causes Hsp-70·ADP to bind tightly to the precursor, as shown in state 2. The transition 2→3 occurs when Pi is released, which in turn triggers the power stroke. The transition 3→4 is driven by both thermal diffusion and a power stroke, which has been schematically depicted as arising from the release of energy stored in an elastic element. After the power stroke is complete and the Hsp-70·ADP nearest the membrane has fluctuated out of the way (shown schematically in state 4 as a 180° rotation), another Hsp-70·ATP is free to associate with the channel complex and precursor. As shown in the figure, the transition rate for this process is k_{01}. The cycle then starts again. The release of Hsp-70 from the precursor is not shown in the figure. However, this event is allowed in the model and characterized by the dissociation rate k_{10}. (*B*) The mechanochemical cycle of the Brownian ratchet. The chemical steps in this figure are identical with those of Fig. 1 *A*. The difference between the two models is in the transition 3→4. As shown in the figure, for the Brownian ratchet, this transition is driven by biased thermal diffusion alone.

sumptions do not seem unreasonable, because they involve steps in the cycle in which Hsp-70 is already bound to the channel complex. This allows the binding site nearest the membrane, and all subsequent sites along the precursor, to be described by two chemical states determined by the presence or absence of Hsp-70. In Fig. 1, *A* and *B*, the boxes indicate the two states for the binding site nearest the membrane. The specification of the chemical state of the entire precursor requires knowing the chemical state of each binding site within the organelle (see below). However, we will refer to the precursor as being in the "empty" state when Hsp-70 is not bound to the first site and as being in the "occupied" state if the first site has Hsp-70 bound to it. Note that there are two mechanisms that change the chemical state of the site nearest the membrane. The first possibility is a chemical step involving the association or dissociation of Hsp-70, and the second is a physical step in which the position of the precursor changes. The difference between the two models lies solely with the latter step. The specific details of the chemical kinetics we have chosen may not be correct. However, a useful property of the mathematical description given in the next section is that, as more information about the chemical kinetics becomes available, it is straightforward to include these details in the analysis. Because the chemistry of each model is identical, the addition of new chemical steps will affect the models equivalently, and not alter the qualitative differences reported in this paper.

MATHEMATICAL FRAMEWORK

In the empty state of both models, the force balance for the precursor is

$$F_V = F_B + F_l, \quad (1)$$

where F_V is the force due to viscous drag, F_B is the force due to thermal fluctuations, and F_l represents any experimentally applied forces. The relationship between the viscous drag and velocity, v, is $F_V = \xi v$, where ξ is the friction coefficient. For the power stroke model, the force balance in the occupied state is

$$F_V = F_p + F_B + F_R + F_l, \quad (2)$$

where F_p is the power stroke and F_R is the ratchet force exerted when steric hindrance prevents the chain from moving back through the pore. In general, $F_p = -\partial\phi(x)/\partial x$, where the potential $\phi(x)$ must be specified. In the Results, two specific forms of $\phi(x)$, linear and quadratic, are considered. The performance of the two functional forms is shown to be approximately equal. Because F_R is short ranged, it is modeled through use of a reflecting boundary condition. For the Brownian ratchet, the force balance is the same as the power stroke model except that $F_p = 0$. Therefore, the Brownian ratchet is a limiting case of the power stroke model. However, for clarity we analyze the two models separately.

Figure 1, *A* and *B*, only show a small segment of the precursor. In general, Hsp-70 can be bound anywhere along the portion of the precursor that is within the organelle. We will use 0 to denote an empty site and 1 to denote an occupied site. The channel complex may catalyze the binding of Hsp-70 to the precursor. If this is the case, the rate constants for the first site will be different from those further along the chain. However, we will make the simplifying assumption that the association and dissociation rates are the same along the entire precursor protein. These will be denoted as k_{01} and k_{10} for association and dissociation, respectively. It is straightforward to incorporate different rate constants for the first site in our theory. Including this effect will not alter the results of the various approximations discussed below, because, for sites away from the membrane, only the ratio of the transition rates is required, and this ratio must be k_{01}/k_{10}.

Figure 2 shows a portion of the state diagram for the precursor. In this figure, N is the number of sites that have entered the organelle. In each circle, the sequence of zeros and ones indicates the state of the binding sites along the chain, starting with the site nearest the membrane. Therefore, the chemical state of the precursor is specified by the N-dimensional vector $\mathbf{y}^{(N)}$, whose components are either 0 or 1. The horizontal arrows represent transitions that move the precursor by one site. In the Brownian ratchet this is accomplished by diffusion, and, in the power stroke model, forward transitions are aided by a power stroke. Note that,

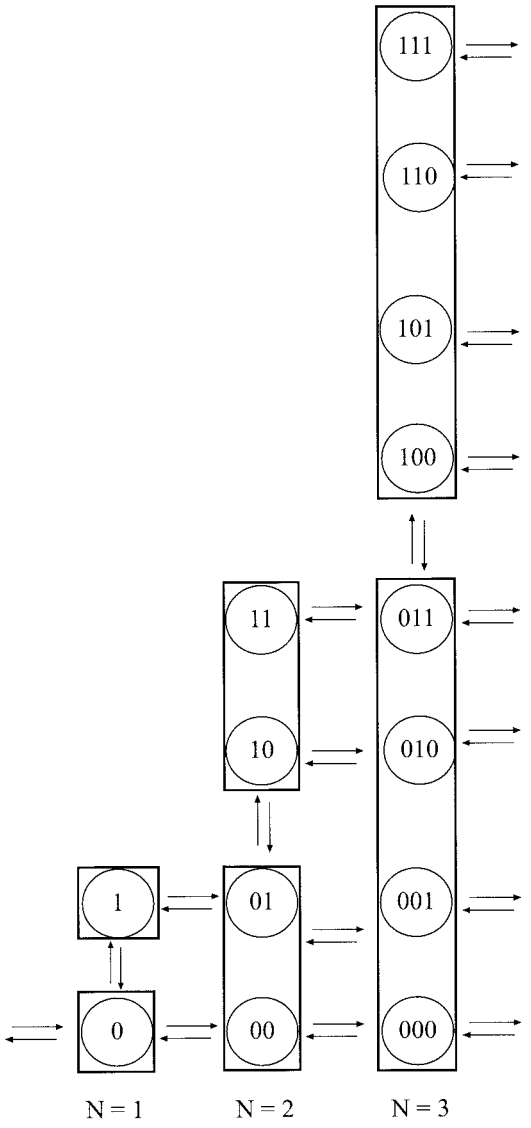

FIGURE 2 A portion of the state diagram for the precursor protein. N is the number of binding sites that have entered the organelle. The state of each binding site within the organelle is represented by 0 or 1 depending on whether that site is empty or occupied, respectively. Transitions that require a physical motion of the precursor are denoted by horizontal arrows, and the vertical arrows denote chemical transitions that change the state of the binding site nearest the membrane.

to simplify the diagram, not all the transitions between states for a single value of N have been labeled. However, all transitions between states that differ by only one value of 0 or 1 are allowed. Figure 3 shows a schematic diagram of the mathematical model we will study. As shown in the figure, the precursor is considered to be rigid. In the Discussion, we argue the validity of this assumption. There is evidence that precursors with partially folded domains can be translocated into mitochondria and that these domains are unfolded before translocation occurs (Voisine et al., 1999; Schwartz et al., 1999). Currently, our theory does not

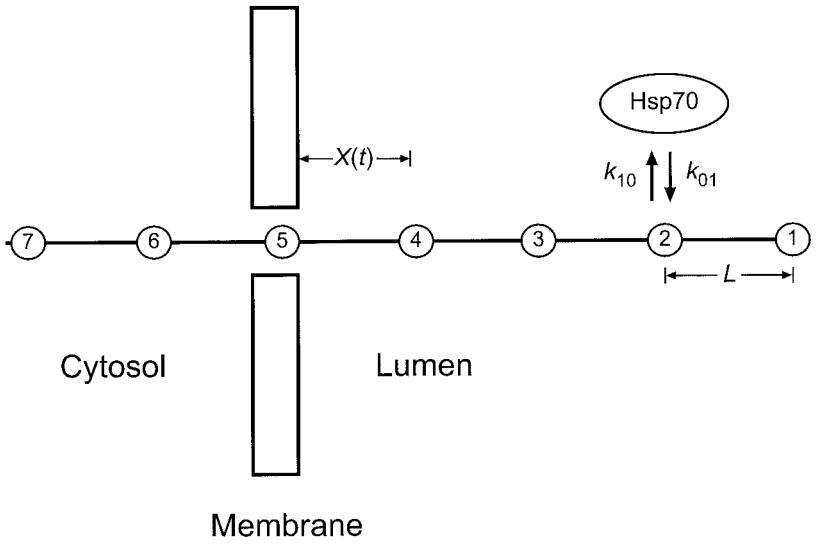

FIGURE 3 A diagram of the mathematical model. The variable x denotes the distance between the membrane and the nearest binding site. Hsp-70 can bind to any site that is within the organelle. The association rate k_{01} and dissociation rate k_{10} are constant for all sites along the precursor. This assumption does not affect the three approximations, because, for sites other than the one nearest the membrane, only the ratio k_{10}/k_{01} is needed. The precursor is assumed to be rigid and the binding sites, which are depicted as circles, are evenly spaced apart by a distance L.

address protein folding and, therefore, is not applicable to precursors that contain folded domains. We also assume that the binding sites along the precursor are equally spaced apart by a distance L. This may not be the case. However, if the distance between binding sites is small compared to the length of the precursor, then L represents the mean distance between sites. The distance between the membrane and the closet binding site is x. The state of the protein is completely specified by N, x, and $\mathbf{y}^{(N)}$. There are 2^N possibilities for $\mathbf{y}^{(N)}$. Let $\boldsymbol{\rho}(x, N)$ be a 2^N dimensional vector whose ith element is the probability density for being at position x, with N sites translocated, and the states of the N sites being given by $\mathbf{y}^{(N)}$. We can divide $\boldsymbol{\rho}(x, N)$ into two vectors of dimension 2^{N-1}

$$\boldsymbol{\rho}(x, N) = \begin{pmatrix} \boldsymbol{\rho}_0(x, N) \\ \boldsymbol{\rho}_1(x, N) \end{pmatrix}, \tag{3}$$

where the subscripts 0 and 1 refer to the state of the site nearest the membrane. In Fig. 2, the states in the lower rectangles comprise $\boldsymbol{\rho}_0$, and those in the upper rectangles comprise $\boldsymbol{\rho}_1$. In Appendix A, we show that the Fokker–Planck equations for the marginal densities $\rho_0(x, t)$ and $\rho_1(x, t)$, which are constructed by summing $\boldsymbol{\rho}_0$ and $\boldsymbol{\rho}_1$ over their elements and all values of N, are given by

$$\frac{\partial \rho_0}{\partial t} = D\left(\frac{\partial^2 \rho_0}{\partial x^2} + \frac{F_1}{kT}\frac{\partial \rho_0}{\partial x}\right) - k_{01}\rho_0 + k_{10}\rho_1, \tag{4}$$

$$\frac{\partial \rho_1}{\partial t} = D\left(\frac{\partial^2 \rho_1}{\partial x^2} + \frac{1}{kT}\frac{\partial}{\partial x}\left(F_1 + \frac{\partial \phi}{\partial x}\right)\rho_1\right) - k_{10}\rho_1 + k_{01}\rho_0. \tag{5}$$

The diffusion coefficient $D = kT/\xi$, where k is the Boltzmann constant and T is the absolute temperature. The total flux J for this system is

$$J = -D\left(\frac{\partial}{\partial x}(\rho_0 + \rho_1) + \frac{F_1}{kT}(\rho_0 + \rho_1) + \frac{1}{kT}\left(\frac{\partial \phi}{\partial x}\right)\rho_1\right). \tag{6}$$

One quantity of interest is the mean velocity of the precursor. To find the average velocity, Eqs. 4 and 5 are solved in steady state. That is, with their left-hand side set equal to 0. In this case, J is a constant and related to the mean velocity by $v = JL$, where L is the distance between binding sites. To determine J, the appropriate boundary conditions must be specified.

Boundary conditions

As shown in Appendix A, the appropriate steady-state boundary and normalization conditions are

$$\left[\frac{\partial \rho_1}{\partial x} + \frac{1}{kT}\left(F_1 + \frac{\partial \phi}{\partial x}\right)\rho_1\right]_{x=0} = 0, \tag{7}$$

$$\rho_0(0) = \rho_0(L) + \rho_1(L), \tag{8}$$

$$\rho_0(L) = \alpha\rho_0(0), \tag{9}$$

$$\int_0^L (\rho_0 + \rho_1)\, dx = 1. \tag{10}$$

Eq. 7 is a reflecting boundary condition. It models the fact that a site with Hsp-70 bound to it cannot pass back through the membrane. Referring to Fig. 2, the parameter α in Eq. 9 is interpreted in the following way. If the precursor moves backward and the first binding site is empty, then this site can pass back through the membrane. In which case, the second binding site becomes the first. The parameter α is the probability that the second binding site is empty when

this transition occurs. That is, α is the conditional probability for the binding site nearest the membrane to be empty given that $x = L$. In general, this probability cannot be found with out solving the full problem. That is, determining the joint densities given in Eq. 3. However, α can be approximated using various different assumptions.

Three approximations

In this section, we discuss three different approximations that are used to construct asymptotic solutions for the average velocity and effective diffusion coefficient. As discussed in the Discussion, strong precursor–pore interactions greatly reduce the diffusion coefficient of the precursor. Therefore, the underlying assumption of the different approximations is that the time scale set by thermal diffusion L^2/D is long compared to the time scale set by the chemical kinetics $1/k_{10}$ and $1/k_{01}$. The approximations are presented in order of increasing accuracy, and, in the Results, the validity of each approximation is addressed by direct comparison with Monte-Carlo simulations of the full problem. In Appendix B, the solutions obtained under each approximation are discussed.

Fast kinetics approximation

The first approximation we consider is the one studied by Simon et al. (1992) and Peskin et al. (1993), and is referred to as the fast kinetics approximation. They studied the problem in the limit that k_{01} and $k_{10} \to \infty$ with their ratio remaining finite. Physically, this means that, as soon as a binding site enters the organelle from the pore, it is in chemical equilibrium. That is, the probability that any given site is empty is $k_{10}/(k_{10} + k_{01})$. In this limit $\rho_1(x, t) = k_{01}/k_{10}\rho_0(x, t)$, and the steady-state flux satisfies the equation

$$J = -D\left(\frac{\partial \rho}{\partial x} + \frac{1}{kT}\left(F_1 + \frac{k_{01}}{k_{01} + k_{10}}\frac{\partial \phi}{\partial x}\right)\rho\right), \qquad (11)$$

where $\rho(x)$ is the marginal density defined as $\rho(x) = \rho_1(x) + \rho_0(x)$, and $k_{01}/(k_{01} + k_{10})$ is the equilibrium probability for an occupied site. To determine the mean velocity, Eq. 11 must be solved subject to boundary and normalization condition,

$$\rho(L) = \frac{k_{10}}{k_{10} + k_{01}}\rho(0), \qquad (12)$$

$$\int_0^L \rho(x)\, dx = 1, \qquad (13)$$

which follow from Eqs. 7–10.

The fast kinetics approximation has a simple physical interpretation. In this limit, we can consider the precursor to be moving down the free energy profile shown in Fig. 4. For simplicity in this figure, the power stroke is assumed to arise from a constant force with magnitude $\Delta G_{PS}/L$. The validity of this assumption is discussed in the Results. Each time a new binding site enters the organelle, there is a drop in free energy due to the binding of Hsp-70. This free energy barrier is responsible for ratcheting the precursor and has a height of $\Delta G_{BR} = -kT \ln(k_{10}/(k_{10} + k_{01}))$.

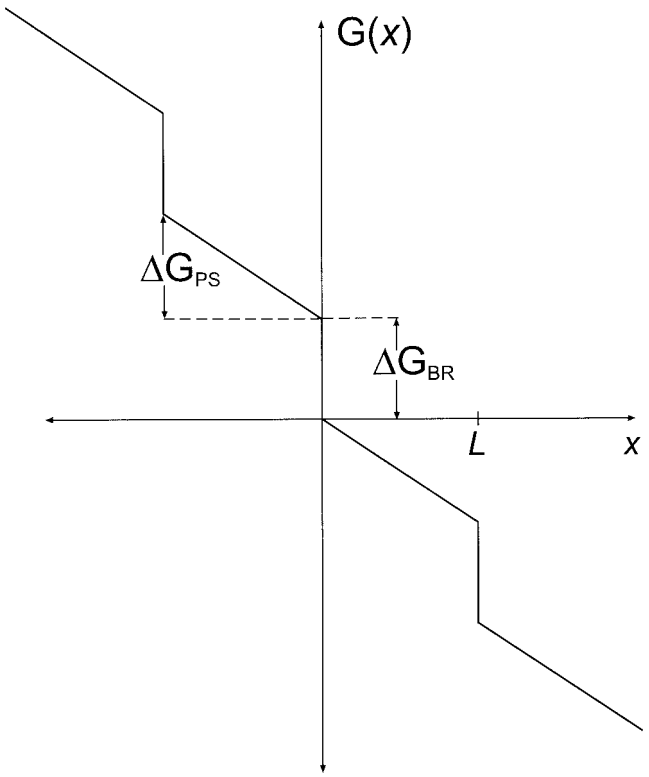

FIGURE 4 The free energy diagram for the precursor in the fast kinetics approximation. In this figure the power stroke generates a constant force $\Delta G_{PS}/L$. Each time a binding site enters the organelle, there is a drop in free energy $\Delta G_{BR} = -kT \ln(k_{10}/(k_{10} + k_{01}))$, due to the binding of Hsp-70, that ratchets the precursor.

Second site approximation

A better approximation is obtained if we assume that it is not the first binding site from the membrane but the second that is in chemical equilibrium. In this case, $\alpha = k_{10}/(k_{10} + k_{01})$, and Eq. 9 becomes

$$\rho_0(L) = \frac{k_{10}}{k_{10} + k_{01}}\rho_0(0). \qquad (14)$$

Whenever a new site enters the organelle it must be unoccupied. Therefore, in general, α will not be equal to the equilibrium probability for an empty site, but will depend on the velocity of the precursor.

Velocity-dependent approximation

The final approximation we consider takes into account the velocity dependence of α in the following way. Solve Eqs.

4 and 5 in steady state and subject to Eqs. 7–10. At this point, α is an unknown parameter. Therefore, the average velocity is a function of α, i.e., $v = v(\alpha)$. To get an expression for α, solve the following set of differential equations for a two-state process:

$$\frac{dp_0}{dt} = -k_{01}p_0 + k_{10}p_1, \tag{15}$$

$$\frac{dp_1}{dt} = -k_{10}p_1 + k_{01}p_0, \tag{16}$$

subject to normalization and initial conditions,

$$p_0 + p_1 = 1, \tag{17}$$

$$p_0(0) = 1. \tag{18}$$

Eq. 18 comes from the fact that, when a binding site enters the organelle, it is unoccupied. The solution to Eq. 15 is

$$p_0 = \frac{k_{01}}{k_{01} + k_{10}} \exp(-(k_{01} + k_{10})t) + \frac{k_{10}}{k_{10} + k_{01}}. \tag{19}$$

Remember that α is the conditional probability for being in the empty state given that $x = L$. The average amount of time it takes for a site to move a distance L is L/v. Therefore, α can be found by setting it equal to p_0 evaluated at $t = L/v$. However, this leads to an expression for α that involves v, the quantity we are trying to find. Therefore, when α is substituted into the expression for the average velocity, we are left with a transcendental equation, which is then solved numerically. This method is an approximation, because it neglects fluctuations in the velocity. For the Brownian ratchet, excellent agreement between theoretical and numerical results is found. However, as discussed below for the power stroke model, we do not expect this approximation to be valid for all values of k_{01} and k_{10}.

RESULTS

Using data from mitochondrial translocation systems, Chauwin et al. (1998) estimated the diffusion coefficient for a precursor diffusing through a translocation pore in the absence of ATP to be $D = 2 \times 10^{-15}$ cm^2/s. In units of nanometers, $D = 0.2$ nm^2/s. This value of D is used in several of the results presented below. After completion of the manuscript, we learned that this estimate is probably too small. As pointed out in the Discussion, where this issue is addressed, our numerical simulations reveal that using a more accurate value of D does not change the validity of the second site approximation. Therefore, the qualitative nature of the results presented in this section will be unaffected when more realistic values of D are used. Using Matlack et al.'s (1999) data shown below in Fig. 9 from ER translocation systems, we demonstrate below that D is in the 6–10 nm^2/s range.

We begin our comparison by considering load–velocity plots for both models. That is, we assume that a constant force, which opposes importation, is applied to the precursor and that the mean velocity is measured as a function of this force. Current experimental techniques do not allow such a load force to be applied. However, the results are useful for illustrating mechanical differences between the models and for testing the validity of the three approximations discussed above. Initially to compare the models, we will consider $D = 1$ nm^2/s and a stall force of 3 pN. In Appendix B, it is shown that, under all three approximations, the stall force F_0 of the Brownian ratchet is

$$F_0 = \frac{kT}{L} \ln\left(1 + \frac{1}{K'}\right), \tag{20}$$

where $K' = k_{10}/k_{01}$. Numerical simulations indicate that Eq. 20 is true in general (see Fig. 5 *A*). Using $L = 3$ nm, roughly the footprint of Hsp-70, and $kT = 4.2$ pN-nm in the above equation produces a value of $K' = 0.13$. In Appendix B, it also is shown that, in the fast kinetics approximation, the stall force of the power stroke model is

$$F_0 = \frac{kT}{L} \ln\left(1 + \frac{1}{K'}\right) + \frac{1}{1 + K'} F_P, \tag{21}$$

where a constant effective power stroke F_p has been assumed. Eq. 21 has a very simple interpretation. It is just the stall force of the Brownian ratchet plus the average force generated by the power stroke. This is what we would predict based on equilibrium arguments. However, we will show that, contrary to the Brownian ratchet, this result is not true in general. If we use the same value of K' as used for the Brownian ratchet and let $F_p = 2$ pN, then solving Eq. 21 for L produces $L = 7.29$. This value of L is useful for comparing the models' performance, because it results in stall forces and average velocities that are similar to those of the Brownian ratchet with $L = 3$ nm. However, no biological significance should be attached to it. If we assume that the power stroke is actually the result of a linear spring with a rest length of 7.29 nm, the value of the spring constant κ needed to produce an average force of 2 pN is $\kappa = 2 \times (2 \text{ pN})/(7.29 \text{ nm}) = 0.55$ pN/nm.

Fig. 5, *A–C* are load–velocity plots for the three different cases described above. In all the figures, the different curves represent different values of k_{01} and k_{10} that have been chosen so that their ratio $K' = k_{10}/k_{01} = 0.13$ remains fixed. Fig. 5 *A* shows the results for the Brownian ratchet. The upper solid line is the fast kinetics approximation (Eq. B1 of Appendix B). By the time $k_{01} = 500$ s^{-1} all three approximations are indistinguishable and lie on the solid line. The dashed lines are the second-site approximation (Eq. B4). Starting from the top, the values of k_{01} used to produce these curves are 10 s^{-1}, 1 s^{-1}, and 0.01 s^{-1}. The data points shown are the results of Monte-Carlo simulations using the same values of k_{01}. Details of the numerical method used to

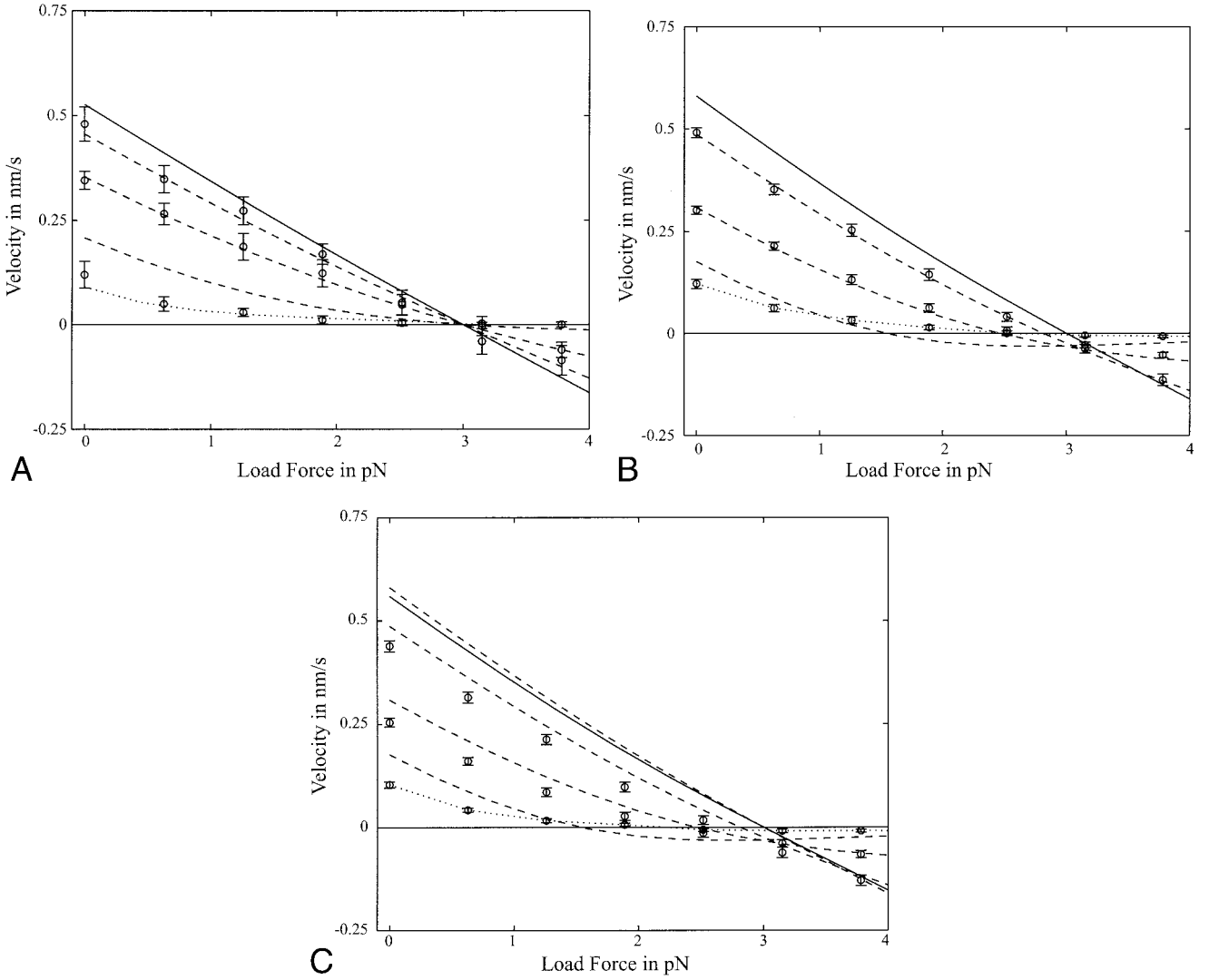

FIGURE 5 (*A*) Load–velocity plots for the Brownian ratchet at different values of k_{01} and k_{10} with K' held fixed. The solid line is the fast-kinetics approximation, the dashed lines are the second-site approximation, the dotted line is the velocity-dependent approximation, and the data points are the results of Monte-Carlo simulations. In this figure, $D = 1$ nm^2/s, $L = 3$ nm, and $K' = 0.13$. (*B*) Load–velocity plots for the power stroke model with a constant power stroke at different values of k_{01} and k_{10} with K' held fixed. The solid line is the fast kinetics approximation, the dashed lines are the second-site approximation, the dotted line is a guide for the eye, and the data points are the results of Monte-Carlo simulations. In this figure, $D = 1$ nm^2/s, $L = 7.29$ nm, $K' = 0.13$, and $F_p = 2$ pN. (*C*) Load–velocity plots for the power stroke model with a linear spring providing the power stroke at different values of k_{01} and k_{10} with K' held fixed. The solid line is the fast-kinetics approximation. The uppermost dashed line is the fast-kinetics approximation using a constant force 2 pN (i.e., the solid line of (*B*). The lower dashed lines are the same as shown in (*B*), and the dotted line is a guide for the eye. The data points are the results of Monte-Carlo simulations. In this figure $D = 1$ nm^2/s, $L = 7.29$ nm, the spring is characterized by a rest length of 7.92 nm and spring constant of 0.55 pN/nm, and $K' = 0.13$.

generate these points are given in Appendix C. We see excellent agreement between the numerical results and the second site approximation for $k_{01} = 10$ s^{-1} and 1 s^{-1}. For these two cases, the curves produced by the velocity-dependent approximation are indistinguishable from the second-site approximation. However, for $k_{01} = 0.01$ s^{-1}, the second-site approximation is no longer valid. The dotted line shown in Fig. 5 *A* was produced from the velocity-dependent approximation with $k_{01} = 0.01$ s^{-1}. Good agreement between this approximation and the numerics is seen. Note that all the approximations and the numerical results predict the same stall force. Thus, for the Brownian ratchet, the stall force only depends on K', and not the specific values of k_{01} and k_{10}.

Figure 5 *B* shows load–velocity plots for the power stroke model with $F_p = 2$ pN. For this case, the values of k_{01} shown are 1 s^{-1}, 0.1 s^{-1}, and 0.01 s^{-1}. Again, the upper solid line is the fast kinetics approximation (Eq. B18) and the dashed lines are a result of the second-site approximation. Note that, contrary to the Brownian ratchet, the stall

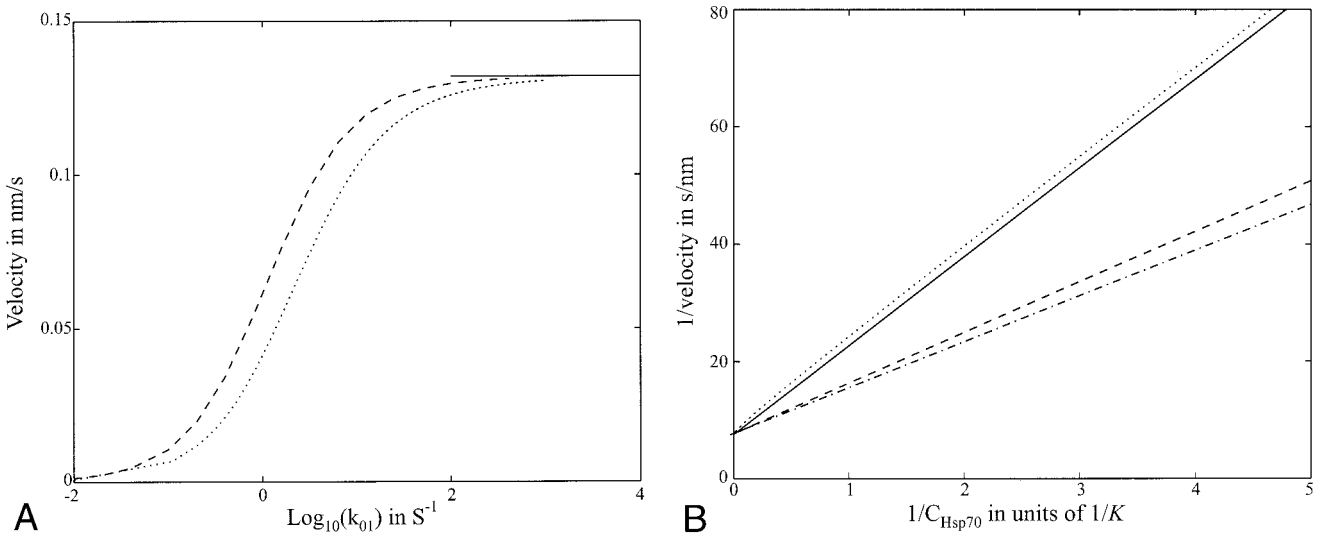

FIGURE 6 (*A*) The mean velocity versus $\log_{10}(k_{01})$. The dashed line is the power stroke model and the dotted line is the Brownian ratchet. In both cases, the limiting velocity is 0.132 nm/s and $k_{10} = 1\ s^{-1}$. (*B*) The inverse of the velocity versus $1/C_{\text{Hsp-70}}$. The solid line is the fast kinetics result for the Brownian ratchet. A real Brownian ratchet produces a steeper slope, as illustrated using the second-site approximation (*dotted line*). A power stroke model produces a smaller slope, as illustrated using the second-site approximation (*dashed line*). The dot-dashed line is the fast-kinetics approximation for the power stroke model.

force does change as k_{01} is varied. Again, by the time $k_{01} = 0.01\ s^{-1}$, the second-site approximation does not accurately capture the behavior of the model. In fact, it grossly underestimates the stall force. In this figure, the dotted line is simply a guide for the eye and not the velocity-dependent approximation. We have not computed this approximation for the power stroke model. However, we expect the velocity-dependent approximation to predict the same stall force as the second-site approximation (see Appendix B), and, therefore, not be valid either. For the power stroke model, the stall force is influenced by the finite transition rates of the chemical kinetics and, therefore, depends explicitly on k_{01}.

Figure 5 *C* shows load–velocity plots for the power stroke model using a linear spring with a spring constant of $\kappa = 0.55$ pN/nm and a rest length of 7.29 nm. The solid line is the fast kinetics approximation (Eq. B15) and the upper dashed line is the fast kinetics approximation for the constant force case. The lower dashed lines are the same as shown in Fig. 5 *B*. As can be seen, the results produced using a constant force compare well with those of the linear spring. This shows that the important parameter is the average or effective force felt during the power stroke. Therefore, from now on, we only consider a power stroke that arises from a constant force.

Figure 6 *A* is a plot of the mean velocity versus the $\log_{10}(k_{01})$ with k_{10} held fixed at $1\ s^{-1}$. In this figure, $D = 0.2\ nm^2/s$ and the second-site approximation was used. The value of L for the Brownian ratchet was taken to be 3.03 nm, so that both models have the same maximum velocity, $v_{max} = 0.132$ nm/s. For the Brownian ratchet, the maximum velocity is $2D/L$ and the maximum velocity of the power stroke model is found from Eq. B20. The shapes of the curves are very similar and seem to indicate that both models obey Michaelis–Menten kinetics. In the fast kinetics limit, the velocity of the Brownian ratchet can be written as

$$v = \frac{v_{max}}{1 + 2K'}. \tag{22}$$

Eq. 22 can be put in Michaelis–Menten form, if we remember that

$$K' = \frac{k_{10}}{k_{01}} = \frac{k_{10}}{k'_{01}\, C_{\text{Hsp70}}} = \frac{K}{C_{\text{Hsp70}}}, \tag{23}$$

where K is the equilibrium constant and $C_{\text{Hsp-70}}$ is the concentration of Hsp-70. Making this substitution in Eq. 22 produces

$$v = \frac{v_{max} C_{\text{Hsp70}}}{2K + C_{\text{Hsp70}}}, \tag{24}$$

where the Michaelis constant $K_M = 2K$. The equilibrium constant and Hsp-70 concentration can be measured using standard biochemical techniques, and, below, we present an experimental method for measuring the average velocity. Thus, a direct comparison of Eq. 24 and experimental data should be possible. A useful way to do this is through use of a Lineweaver–Burk plot. In this case Eq. 24 is rewritten in terms of $1/v$. That is,

$$\frac{1}{v} = \frac{1}{v_{max}} + \frac{2K}{v_{max}}\left(\frac{1}{C_{\text{Hsp-70}}}\right). \tag{25}$$

Figure 6 *B* shows Lineweaver–Burk plots for four different cases. The solid line shown in this figure was produced from Eq. 25. The dotted line represents the second site result for the Brownian ratchet shown in Fig. 6 *A*. Including finite transition rates in the Brownian ratchet model has the effect of increasing the Michaelis constant (greater slope), therefore a Brownian ratchet will always produce results that lie above the solid line. The dashed line corresponds to the result shown in Fig. 6 *A* for the power stroke model. Its slope is less than the one produced by Eq. 25. To approximate the results for the power stroke model, Eq. B18 for the average velocity in the fast kinetics approximation, is expanded to first order in $1/C_{\text{Hsp-70}}$. The result is

$$\frac{1}{v} = \frac{1}{v_{\max}} + \frac{K(1 + e^{-(F_p L/kT)})}{v_{\max}} \left(\frac{1}{C_{\text{Hsp-70}}}\right) + O(C_{\text{Hsp-70}}^{-2}), \qquad (26)$$

where $v_{\max}$ is now given by Eq. B20. This curve is plotted as the dot-dashed line in Fig. 6 *B*, and compares well with the second-site approximation for the power stroke model. From Eq. 26, we see that the Michaelis constant for the power stroke model can be approximated by

$$K_M = K(1 + e^{-(F_p L/kT)}). \qquad (27)$$

Thus, the effect of the power stroke is to reduce the Michaelis constant from its limiting value of $2K$, which is the approximate result for the Brownian ratchet. Plotting the data as done in Fig. 6 *B* provides a method for distinguishing the two operating principles. If the data lie below the solid line, then a power stroke is involved in translocation, otherwise translocation is driven by thermal fluctuations alone. If a power stroke is involved, then Eq. 27 can be used to estimate its strength.

If in the future it becomes possible to measure the stall force, then the fact that the stall force of the Brownian ratchet only depends on Hsp-70 concentration through the functional form $\ln(1 + C_{\text{Hsp-70}}/K)$ can also be used to differentiate the models. Figure 7 is a plot of the stall force as a function of $\ln(1 + C_{\text{Hsp-70}}/K)$. In this figure, $D = 0.2$ nm^2/s, $k_{10} = 1$ s^{-1}, and $L = 3$ nm for both models, and the strength of the power stroke is $F_p = 2$ pN. The solid line is the second-site approximation for the Brownian ratchet. The dashed line is the second-site approximation for the power stroke model. Using this representation, the curve for the Brownian ratchet is linear with slope kT/L, whereas the power stroke model produces a nonlinear curve. The validity of using the second-site approximation to compute the stall force of the power stroke model may be questionable, because it was shown that the stall force depends explicitly on k_{01}. However, it is hard to imagine that this effect will decrease the nonlinearity shown in the figure, rather than increase it.

Information about the translocation mechanism, which is independent of the mean velocity, is found by studying the variance in precursor position as a function of time. The

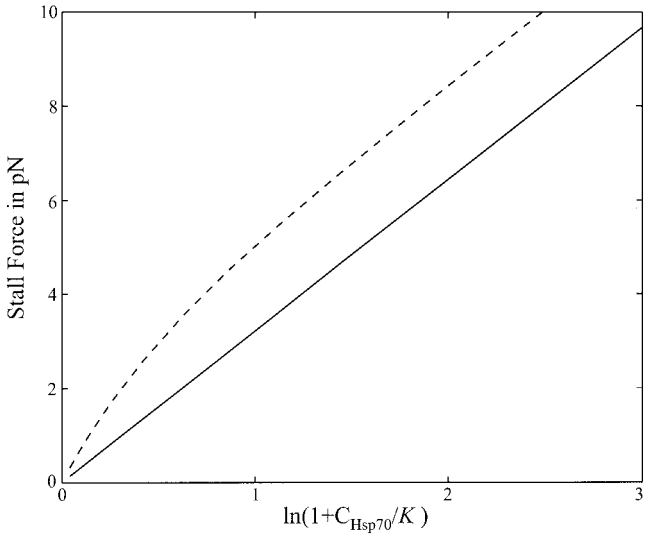

FIGURE 7 The stall force versus $\ln(1 + C_{\text{Hsp-70}}/K)$. The dashed curve is the second-site approximation for the power stroke model and the solid line is the second-site approximation for the Brownian ratchet. In this figure, $F_p = 2$ pN, $D = 0.2$ nm^2/s, $k_{10} = $ s^{-1}, and $L = 3$ nm.

variance is related to the precursor's diffusion coefficient. If the motion of the precursor is viewed on times scales that are longer than $1/k_{01}$, $1/k_{10}$, and L^2/D, then its dynamics can be modeled using the following macroscopic diffusion equation (Lubensky and Nelson, 1999; Elston, 1999; Wang et al., 1998)

$$\frac{\partial \rho}{\partial t} = D_{\text{eff}} \frac{\partial^2 \rho}{\partial x^2} - v \frac{\partial \rho}{\partial x}, \qquad (28)$$

where v is the mean velocity, and D_{eff} is a macroscopic or effective diffusion coefficient. That is, we can view the chain as undergoing diffusion with a constant drift. One contribution to the effective diffusion coefficient comes from pore-precursor interactions (Chauwin et al., 1998). These interactions are present even in the absence of organellar translocation machinery and act to reduce the bare diffusion coefficient of the precursor. The diffusion coefficient D already takes into account pore–precursor interactions. Other effects that will determine the overall value of D_{eff} are the strength of the power stroke and the underlying chemical kinetics. In general, these influences can either increase or reduce the effective diffusion coefficient. A derivation of Eq. 28 and an algorithm for computing D_{eff} from the underlying microscopic dynamics have been presented elsewhere (Elston, 1999).

At very low concentrations of Hsp-70, the effective diffusion coefficient asymptotically approaches that of a precursor passively diffusing through a translocation pore D. As shown in Appendix B, if a Brownian ratchet drives protein translocation, then D_{eff} approaches $\frac{2}{3}D$ as $C_{\text{Hsp-70}}$ is increased. If a power stroke is involved in translocation, then the effective diffusion coefficient is less sensitive to

variations in $C_{\text{Hsp-70}}$. These theoretical considerations are summarized in Fig. 8, which was produced using Eq. B36. In this figure, D_{eff}/D has been plotted as a function of the log of the $K/C_{\text{Hsp-70}}$. The three curves represent different values of the average power stroke generated by Hsp-70. Starting with the lower curve, the values of the average power stroke are 0, 2, and 4 pN. The lower curve represents the Brownian ratchet and approaches $\frac{2}{3}D$ as $C_{\text{Hsp-70}}$ is increased. As the power stroke increases, the curves approach a limiting value of 1. Therefore, the effective diffusion coefficient not only can be used to determine if a power stroke is used during translocation, but it's limiting value at high Hsp-70 concentration also provides a measure of the power stroke's strength.

Measuring the mean velocity and effective diffusion coefficient

The average velocity and effective diffusion coefficient of the two models were shown to behave differently as Hsp-70 concentration was varied. Currently, there is not a straightforward technique for measuring these quantities. However, experimental measurements of the fraction of proteins released from the channel as a function of time have been made. In these experiments, ppαF is initially bound to translocation channels in proteoliposomes. Next, the translocation complex with bound precursor is solubilized in detergent, and translocation is initiated by the addition of ATP and Hsp-70 (Matlack et al., 1997, 1999). As discussed in Appendix D, Eq. 28 can be used to calculate the fraction of released proteins. The two adjustable parameters in this equation are the average velocity and effective diffusion coefficient. The data points shown in Fig. 9 are experimental data for the fraction of ppαF released from the Sec complex as a function of time. These data were taken from Fig. 1 *C* of Matlack et al. (1999). Solutions of Eq. 28 have been used to fit the data using three different values of the average velocity, $v = 0$, 0.1, 0.2 nm/s. For these three velocities, the values of D_{eff} that produced the best fit (by eye) were $D_{\text{eff}} = 10$, 9, and 6 nm^2/s, respectively. It was assumed that ppαF consists of 165 amino acids, and 10 amino acids are approximately 3.5 nm in length. Therefore, the total length of the chain was taken to be $L_p = 58$ nm. Note that all three curves fit the data well. For velocities of >0.2 nm/s, the data did not fit well, because, at higher velocities, the slope of the theoretical curve becomes too steep. To uniquely determine the average velocity and effective diffusion coefficient, another data set is needed. However, the new data must be generated in a way that does not change the values of v and D_{eff}. One possibility is to increase the length of the translocating chain. This can be accomplished by synthesizing a protein that consists of two repeats of ppαF, thereby ensuring that the statistical properties of the precursor (e.g., the average length between sites for Hsp-70 binding, glycosylation, and disulfide bound formation) are preserved. The three curves shown in the inset of Fig. 9 were produced using the same parameters as in the figure, except that L_p was increased to 100 nm. The curves are now distinguishable and can be compared against experimental data to determine the average velocity and effective diffusion coefficient.

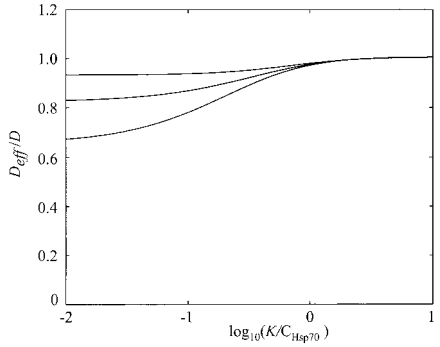

FIGURE 8 The effective diffusion coefficient versus $\log_{10}(K/C_{\text{Hsp-70}})$. The lower curve represents the Brownian ratchet, and the two upper curves are for the power stroke model with F_p equal to 2 and 4 pN, going from bottom to top.

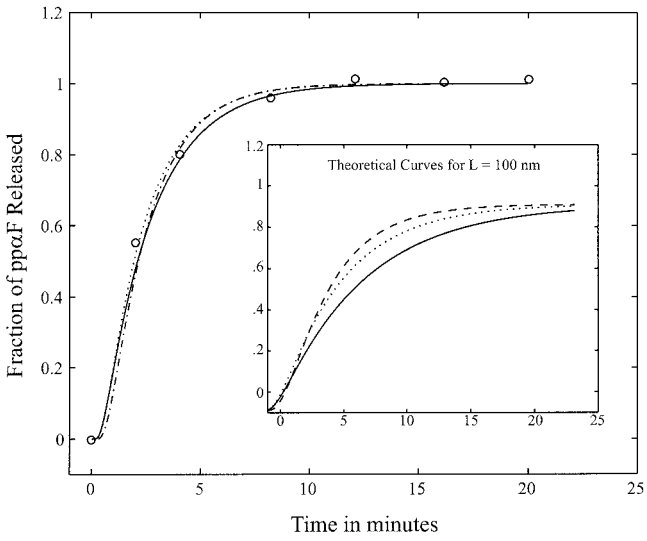

FIGURE 9 Fraction of protein released from the channel as a function of time. The data points were taken from Matlack et al. (1999). In this experiment, the concentration of BiP was 1 μM. The solid curve was produced using $v = 0$, the dotted curve was produced using $v = 0.1$ nm/s, and the dashed curve was produced using $v = 0.2$ nm/s. *Inset*: same as the figure except the length of the precursor has been increased to 100 nm.

DISCUSSION

A mathematical analysis of the Brownian ratchet and power stroke models of post-translational translocation was presented. The investigations focused on two statistically independent quantities, the mean velocity of the precursor and

its variance in position. Analytical approximations were obtained for these quantities under the simplifying assumption that the chemical kinetics of the system is fast as compared with the diffusive motion of the precursor. This assumption was initially based on the work of Chauwin et al. (1998). Using data from the backsliding experiments of Ungermann et al. (1996), they calculated an effective diffusion coefficient of 0.2 nm^2/s, and several of the results presented above are based on this value. After completing the manuscript, we became aware of the work of Liebermeister, W., T. Rapoport, and R. Heinrich (submitted for publication) that shows the rate-limiting step in the backsliding experiments is the release of Hsp-70. Therefore, Ungermann et al.'s data do not provide information about precursor–pore interactions. The data shown in Fig. 9 do not suffer from this constraint, because, in this experiment, the precursor is moving in the forward direction (i.e., from the cytoplasm to the lumen). Using this data, we have shown that the effective diffusion coefficient is between 6 and 10 nm^2/s, which is still well below the value of protein diffusing freely through a channel, and the average velocity is in the range of 0.1–0.2 nm/s. The model studied by Liebermeister et al. uses a Markov chain to describe the precursor. Their model predicts an effective diffusion coefficient and average velocity of approximately 5 nm^2/s and 0.3 nm/s, respectively, which compares well with our results. To fit the data, Liebermeister et al. used $k_{01} \approx 1\ s^{-1}$ at Hsp-70 concentrations of 1 μM. Our numerical simulations reveal that, when $D = 1\ nm^2/s$, the second-site approximation is still valid when k_{01} is as small as $0.1\ s^{-1}$. The validity of the second-site approximation is determined by the value of the dimensionless quantity $D/(k_{01}L^2)$. Thus, increasing both D and k_{01} by a factor of ten will not affect the validity of this approximation, thereby justifying its use.

We have focused our analysis on differences between the models that can be observed as $C_{\text{Hsp-70}}$ is varied because this is an experimentally controllable quantity. The results depend on being able to measure the mean velocity and effective diffusion coefficient of the precursor. We showed that these two quantities can be inferred by using data from current experimental techniques. The procedure for doing this is a generalization of the method proposed by Chauwin et al. (1998), which depends on measuring the fraction of precursor protein released from the membrane as a function of time. The mean velocity of both models produced Michaelis–Menten kinetics. However, the Michaelis constant, which affects the slope of a Lineweaver–Burk plot, is different in each case. For the power stroke model, the Michaelis constant is approximately $K(1 + \exp(-F_pL/kT))$ and is always less than $2K$, the approximate result for the Brownian ratchet. Therefore, the power stroke model approaches its limiting velocity faster than the Brownian ratchet as $C_{\text{Hsp-70}}$ is increased. The variance in the precursor's position is related to the diffusion coefficient. If the translocation system is viewed on lengths scales that are long compared to the distance between binding sites and time scales that are slow compared to those set by chemical kinetics and thermal diffusion, then the system is well approximated by diffusive motion with constant drift. In this approximation, the effective diffusion coefficient depends on the underlying chemical kinetics, the reduced diffusion coefficient of the precursor that takes into account pore–precursor interactions, and the mechanism driving translocation. For the Brownian ratchet, the effective diffusion coefficient approaches $\frac{2}{3}D$ as $C_{\text{Hsp-70}}$ is increased, whereas the power stroke model is less sensitive to variations in $C_{\text{Hsp-70}}$.

The mathematical models presented here are simplistic and lack many biochemical and biophysical details. One important property that has been neglected is protein flexibility. Throughout this work, the precursor was treated as a rigid rod. This assumption greatly simplified the mathematical models and allowed analytical formulae for the mean velocity and effective diffusion coefficient to be derived. To incorporate protein flexibility into the model, the precursor can be modeled as a series of beads connected by springs (Simon et al., 1992). A complete analysis of this problem requires numerical simulations and is the focus of ongoing research. Here we present arguments based on physical reasoning to support the simplifying assumption of precursor rigidity. Clearly, incorporating protein flexibility into the model will affect pore–precursor interactions. However, these types of interactions are already accounted for in the diffusion coefficient D, and therefore will not change the results presented in this manuscript. It is also possible that using an extensible precursor will alter the performance of the two mechanisms. A flexible precursor could improve the performance of the Brownian ratchet, because, in this case, a thermal fluctuation can stretch the precursor and allow Hsp-70 to bind before the length of a full binding site has diffused through the channel. We expect this effect to be small and, to a first approximation, simply reduce the model parameter L. Therefore, the results for the Brownian ratchet should not qualitatively change. As pointed out by Chauwin et al. (1998), protein flexibility could significantly improve the performance of the power stroke model. The reason for this is that, with an extensible precursor, multiple precursor–pore interactions can be broken sequentially, rather than simultaneously as is required for the rigid precursor. If this is indeed the case, we expect the differences between the two models presented here to be accentuated. Again we stress that to fully understand the role of protein flexibility requires numerical analysis and will be the subject of future investigations. Other areas for future work are to incorporate the related effect of protein folding into the model and include more biochemical details in the chemical kinetics. These effects are important for quantitatively matching experimental data and provide further physical insight into the translocation process (Liebermeister et al., submitted). However, we believe that the models presented here capture

the relevant features for distinguishing the Brownian ratchet and power stroke model and that the qualitative nature of the results will not change as more biological details are incorporated into the models.

APPENDIX A: THE BOUNDARY CONDITIONS

By considering Fig. 2, the Fokker–Planck equation for the joint densities given in Eq. 3 is found to be

$$\frac{\partial}{\partial t}\boldsymbol{\rho}_0(x,N,t) = D\left(\frac{\partial^2}{\partial x^2}\boldsymbol{\rho}_0(x,N,t) + \frac{F_1}{kT}\frac{\partial}{\partial x}\boldsymbol{\rho}_0(x,N,t)\right) + \mathbf{K}\boldsymbol{\rho}_0(x,N,t) - k_{01}\boldsymbol{\rho}_0(x,N,t) + k_{10}\boldsymbol{\rho}_1(x,N,t), \tag{A1}$$

$$\frac{\partial}{\partial t}\boldsymbol{\rho}_1(x,N,t) = D\left(\frac{\partial^2}{\partial x^2}\boldsymbol{\rho}_1(x,N,t) + \frac{1}{kT}\frac{\partial}{\partial x}\left(F_1 + \frac{\partial\phi}{\partial x}\right)\boldsymbol{\rho}_1(x,N,t)\right) + \mathbf{K}\boldsymbol{\rho}_1(x,N,t) - k_{10}\boldsymbol{\rho}_1(x,N,t) + k_{01}\boldsymbol{\rho}_0(x,N,t), \tag{A2}$$

where $\mathbf{K}$ is a $2^{N-1} \times 2^{N-1}$ transition matrix that governs transitions for all the binding sites along the precursor, except the one nearest the membrane. Again, from studying Fig. 2, we see that the boundary conditions are

$$\boldsymbol{\rho}_0(0,N,t) = \begin{pmatrix}\boldsymbol{\rho}_0(L,N-1,t)\\ \boldsymbol{\rho}_1(L,N-1,t)\end{pmatrix}, \tag{A3}$$

$$\mathbf{J}_0(0,N,t) = \begin{pmatrix}\mathbf{J}_0(L,N-1,t)\\ \mathbf{J}_1(L,N-1,t)\end{pmatrix}, \tag{A4}$$

$$\mathbf{J}_1(0,N,t) = 0. \tag{A5}$$

Define the marginal densities $\rho_0(x,N,t)$ and $\rho_1(x,N,t)$ as

$$\rho_0(x,N,t) = \sum_{i=1}^{2^{N-1}} (\rho_0(x,N,t))_i, \tag{A6}$$

$$\rho_1(x,N,t) = \sum_{i=1}^{2^{N-1}} (\rho_1(x,N,t))_i, \tag{A7}$$

where the sums are over all elements of $\boldsymbol{\rho}_0$ and $\boldsymbol{\rho}_1$. In terms of the marginal densities, the Fokker–Planck equation becomes

$$\frac{\partial\rho_0(x,N,t)}{\partial t} = D\left(\frac{\partial^2\rho_0(x,N,t)}{\partial x^2} + \frac{F_1}{kT}\frac{\partial\rho_0(x,N,t)}{\partial x}\right) - k_{01}\rho_0(x,N,t) + k_{10}\rho_1(x,N,t), \tag{A8}$$

$$\frac{\partial\rho_1(x,N,t)}{\partial t} = D\left(\frac{\partial^2\rho_1(x,N,t)}{\partial x^2} + \frac{1}{kT}\frac{\partial}{\partial x}\left(F_1 + \frac{\partial\phi}{\partial x}\right)\rho_1(x,N,t)\right) - k_{10}\rho_1(x,N,t) + k_{01}\rho_0(x,N,t), \tag{A9}$$

and using Eqs. A3–A5, the boundary conditions are

$$\left[\frac{\partial\rho_1(x,N,t)}{\partial x} + \frac{1}{kT}\left(F_1 + \frac{\partial\phi}{\partial x}\right)\rho_1(x,N,t)\right]_{x=0} = 0, \tag{A10}$$

$$\rho_0(0,N,t) = \rho_0(L,N-1,t) + \rho_1(L,N-1,t), \tag{A11}$$

$$J_0(0,N,t) = J_0(L,N-1,t) + J_1(L,N-1,t). \tag{A12}$$

Note that, for any given value of N, we are left with only 3 boundary conditions. Because Eqs. A8 and A9 are second order in spatial derivatives, in general, we need 4 conditions. It is not surprising that, by working with the marginal densities, we have lost information about the system. The problem is with Eq. A11. When working with marginal densities, if an empty site moves back into the pore, we are unable to determine if the second site, which then becomes the first, was occupied or empty. The information that we are lacking is the conditional probability for the first site being unoccupied given that $x = L$. Denote this probability as $\alpha(t)$. Then the final condition we require is

$$\rho_0(L,N-1,t) = \alpha(t)\rho_0(0,N,t). \tag{A13}$$

If we now sum over all N, we are left with Eqs. 4 and 5, and the boundary conditions become

$$\left[\frac{\partial\rho_1(x,t)}{\partial x} + \frac{1}{kT}\left(F_1 + \frac{\partial\phi}{\partial x}\right)\rho_1(x,t)\right]_{x=0} = 0, \tag{A14}$$

$$\rho_0(0,t) = \rho_0(L,t) + \rho_1(L,t), \tag{A15}$$

$$\rho_0(L,t) = \alpha(t)\rho_0(0,t), \tag{A16}$$

$$J_0(0,t) = J_0(L,t) + J_1(L,t). \tag{A17}$$

In steady state, the flux is a constant, and Eq. A17 will automatically be satisfied. For this case, the normalization condition given by Eq. 10 is used.

APPENDIX B: APPROXIMATE SOLUTIONS

Average velocity

In this subsection, we use the approximations discussed in the manuscript to derive expressions for the average velocity. We begin by considering the Brownian ratchet. Peskin et al. (1993) found that, in the fast-kinetics approximation, the average velocity of the Brownian ratchet is

$$v = \frac{2D}{L}\left[\frac{1/2\omega_1^2}{\left(\frac{e^{\omega_1}-1}{1-K'(e^{\omega_1}-1)}\right) - \omega_1}\right], \tag{B1}$$

where $\omega_1 = F_1L/kT$ and $K' = k_{10}/k_{01}$. By examining the above equation, we see that, within the fast-kinetics approximation, the stall force is

$$F_0 = \frac{kT}{L}\ln\left(1 + \frac{1}{K'}\right). \tag{B2}$$

The no-load velocity v_{nl}, which is found by taking the limit $F_l \to 0$ in Eq. B1, is

$$v_{nl} = \frac{2D}{L}\frac{1}{1+2K'}. \tag{B3}$$

The maximum velocity of the Brownian ratchet, $v_{max} = 2D/L$, is attained as $K' \to 0$ in the above equation. This is the velocity of a "perfect" Brownian ratchet (Peskin et al., 1993). The perfect Brownian ratchet corresponds to the case in which a binding site is immediately occupied when it enters the organelle and dissociation does not occur. In this case, the height of the free energy barriers shown in Fig. 4 becomes infinite.

Using the second-site approximation, the average velocity becomes

$$v = \frac{2D}{L}\left[\frac{1/2\omega_l^2}{\left(\frac{\beta(e^\beta+1)+\omega_l(e^\beta-1)}{\beta(e^\beta+1)-\omega_l(e^\beta-1)}\right)\left(\frac{e^{\omega_l}-1}{1-K(e^{\omega_l}-1)}\right)-\omega_l}\right], \tag{B4}$$

where

$$\beta = \sqrt{\omega_l^2 + \frac{4L^2}{D}(k_{01}+k_{10})}. \tag{B5}$$

Note that, again, the stall force is given by Eq. B2. The no-load velocity is now

$$v_{nl} = \frac{2D}{L}\frac{1}{\left(2\left[\frac{2(e^\gamma-1)}{\gamma(e^\gamma+1)}+\frac{1}{2}\right]+2K'\right)}, \tag{B6}$$

where

$$\gamma = \sqrt{\frac{4L^2}{D}(k_{01}+k_{10})}. \tag{B7}$$

By comparing Eqs. B3 and B6, not surprisingly, we find that including finite transition rates decreases the average velocity of the precursor. The transcendental equation obtained by using the velocity-dependent approximation is complicated and not enlightening. Therefore, it will not be presented here. However, by examining Eq. 19 with the substitution $t = L/v$, we see that, when $v = 0$, $\alpha = p_0 = k_{10}/(k_{01}+k_{10})$, which is identical with the second-site approximation. Therefore, we again expect the stall force to be given by Eq. B2. In fact, our numerical simulations confirm that Eq. B2 is the stall force for all values of k_{01} and k_{10}.

For the power stroke model, Eqs. 4 and 5 must be solved with nonzero ϕ. We have not succeeded in finding a general solution to these equations. In the Results section, numerical simulations were used to illustrate that the second-site approximation is valid over a wide range of transition rates. Simulations also indicate that the behavior of a quadratic potential (linear elastic force) is approximately equal to that of a linear potential (constant force). We have not considered nonlinear forces. However, should evidence for such an interaction arise, it is straightforward to include this effect in our simulations, but it is not expected that this will lead to qualitatively different behavior. If the power stroke is approximated using a constant force, then the average velocity can be solved in terms of α. To find the solution involves finding the roots of a cubic equation. This was done on *Mathematica.* The general solution is quite complicated and, therefore, not presented here. We do not consider the velocity-dependent approximation for the power stroke model, because, in this case, it does not provide a computational advantage over doing full numerical simulations.

We now restrict ourselves to the fast-kinetics approximation. In this limit, the flux satisfies the ordinary differential equation,

$$J = -D\left(\frac{\partial}{\partial x}\rho + \frac{1}{kT}\left(\frac{\partial\psi(x)}{\partial x}\right)\rho\right), \tag{B8}$$

where

$$\psi(x) = F_l x + \frac{k_{01}}{k_{01}+k_{10}}\phi(x). \tag{B9}$$

The boundary and normalization conditions are

$$\rho(L) = \frac{k_{10}}{k_{10}+k_{01}}\rho(0), \tag{B10}$$

$$\int_0^L \rho(x)\,dx = 1. \tag{B11}$$

Let

$$\Delta\psi = \psi(L) - \psi(0), \tag{B12}$$

$$\beta = e^{-[\psi(x)/kT]}, \tag{B13}$$

$$\gamma = \frac{e^{-(\Delta\psi/kT)}}{e^{-(\Delta\psi/kT)} - \left(1 - \frac{1}{1+K'}\right)}. \tag{B14}$$

Then the average velocity is

$$v = \frac{DL}{\gamma\int_0^L \beta(x)\,dx\int_0^L \beta^{-1}(x)\,dx + \int_0^L \beta(x)\int_0^x \beta^{-1}(x')\,dx'\,dx}. \tag{B15}$$

From Eq. B14, the stall force of the power stroke model in the fast kinetics approximation is found to be

$$F_0 = \frac{kT}{L}\ln[1+1/K'] - \frac{1}{1+K'}\frac{(\phi(L)-\phi(0))}{L}, \tag{B16}$$

where $1/(1+K') = k_{01}/(k_{10}+k_{01}) = p_1^{(e)}$ is the equilibrium probability for a binding site to be occupied.

Next we make the simplifying assumption that $\phi(x) = -F_p x$. That is, a constant force generates the power stroke. In terms of F_p, Eq. B8 can be written as

$$\frac{d\rho}{dx} + \left(\frac{F_l}{kT} - p_1^{(e)}\frac{F_p}{kT}\right)\rho + \frac{J}{D} = 0. \tag{B17}$$

Therefore, the steady-state velocity is found by making the substitution $\omega_l \to \omega_l - p_1^{(e)}\omega_p$ in Eq. B1, where $\omega_p = F_p L/kT$. The result is

$$v = \frac{2D}{L}\frac{\frac{1}{2}(\omega_l - p_1^{(e)}\,\omega_p)^2}{\frac{(e^{\omega_l - p_1^{(e)}\omega_p}-1)}{(1-K'(e^{\omega_l - p_1^{(e)}\omega_p}-1))} - (\omega_l - p_1^{(e)}\,\omega_p)}, \tag{B18}$$

and the no-load velocity is easily found by setting $\omega_l = 0$. Consider the limit in which $k_{01} \to \infty$. In this limit, $p_1^{(e)} \to 1$ and the velocity is

$$\lim_{k_{01}\to\infty} v = \frac{D}{L}(\omega_l - \omega_p)^2 \frac{1}{e^{\omega_l-\omega_p} - 1 - (\omega_l - \omega_p)}. \quad \text{(B19)}$$

The maximum velocity of the power stroke model can now be found by letting $\omega_l = 0$ in the above equation. This produces the result,

$$v_{max} = \frac{D}{L}\omega_P^2 \frac{1}{e^{-\omega_p} + \omega_p - 1}. \quad \text{(B20)}$$

Note that, as $\omega_p \to 0$ in the above expression, we are left with $v_{max} = 2D/L$, which is the mean velocity of a perfect Brownian ratchet. Also, as $\omega_p \to \infty$, the velocity becomes $v_{max} = D\omega_p/L$. So that, for small values of F_p, rectified Brownian motion helps drive translocation, but this effect gets relatively smaller as the power stroke gets stronger. From Eq. B16, we immediately see that, for the case where the power stroke is derived from a constant force, the stall force is

$$F_0 = \frac{kT}{L}\ln\left(1 + \frac{1}{K'}\right) + \frac{1}{1+K'}F_P. \quad \text{(B21)}$$

Therefore, if F_0, K', and L can be experimentally measured, we have a method for approximating the average strength of the power stroke. Again it should be mentioned that Eq. B21 is not true in general, but holds for the case of large k_{01} and k_{10}.

Effective diffusion coefficient

Here we present an outline of the derivation of the effective diffusion coefficient. A detailed discussion of the derivation can be found elsewhere (Elston, 1999). Define the function $f(x, z, t)$ as

$$f(x, z, t) = \sum_{N=0}^{\infty} z^N \rho(x, N, t). \quad \text{(B22)}$$

The function f is related to the moment-generating function and can similarly be used to compute the moments of $N(t)$. The first two moments are

$$E[N(t)] = \int_0^L \frac{df(x, z, t)}{dz}\bigg|_{z=1} dx, \quad \text{(B23)}$$

$$E[N^2(t)] = \int_0^L \frac{\partial^2 f(x, z, t)}{\partial z^2}\bigg|_{z=1} dx + E[N(t)]. \quad \text{(B24)}$$

Using Eqs. A8–A13 and the fast kinetics approximation, the equation satisfied by f and its boundary conditions are found to be

$$\frac{\partial f(x, z, t)}{\partial t} = D\left(\frac{\partial^2 f(x, z, t)}{\partial x^2} - \frac{1}{1+K'}\frac{F_p}{kT}\frac{\partial f(x, z, t)}{\partial x}\right), \quad \text{(B25)}$$

$$f(0, z, t) = z\frac{K'+1}{K'} f(L, z, t), \quad \text{(B26)}$$

$$J(0, z, t) = zJ(L, z, t), \quad \text{(B27)}$$

where F_l has been set equal to zero and the flux J is given by

$$J(x, z, t) = -D\left(\frac{\partial f(x, z, t)}{\partial x} - \frac{1}{1+K'}\frac{F_p}{kT} f(x, z, t)\right). \quad \text{(B28)}$$

If f is written in terms of an eigenfunction expansion, then the characteristic equation that determines the eigenvalues λ_n is

$$\frac{\Lambda_n^{(+)} + \omega}{\Lambda_n^{(-)} + \omega} = \left(\frac{ze^{\Lambda_n^{(-)}} - 1}{1 - ze^{\Lambda_n^{(+)}}}\right)\left(\frac{K'/(K'+1) - ze^{\Lambda_n^{(+)}}}{ze^{\Lambda_n^{(-)}} - K'/(K'+1)}\right), \quad \text{(B29)}$$

where

$$\Lambda_n^{(\pm)} = -\frac{\omega}{2} \pm \frac{1}{2}\sqrt{\omega^2 + \frac{4D\lambda_n}{L^2}}, \quad \text{(B30)}$$

and $\omega = -p_{s1}^{(e)}\omega_p$. The value of λ_n depends on z. If $z = 1$, then $f(x, 1, t) = \rho(x, t)$ and the largest eigenvalue $\lambda_0(1) = 0$ and is associated with the steady-state solution. Let $z = 1 + \varepsilon$. Then $\lambda_0(\varepsilon)$ can be expanded in the power series,

$$\lambda_0(\varepsilon) = \alpha\varepsilon + \frac{\beta}{2}\varepsilon^2 + O(\varepsilon^3). \quad \text{(B31)}$$

The values of α and β can be found by substituting the above expressions for z and $\lambda_0(\varepsilon)$ into Eq. B29 and expanding to order ε^2. It is possible to show that, in the long time limit, the mean and the variance of $N(t)$ satisfy the relations (Elston, 1999)

$$E[N(t)] = \alpha t + O(1), \quad \text{(B32)}$$

$$\sigma^2 = E[N^2(t)] - E[N(t)]^2 = (\alpha + \beta)t + O(1), \quad \text{(B33)}$$

from which the mean velocity and effective diffusion coefficient are found to be

$$v = L\alpha, \quad \text{(B34)}$$

$$D_{eff} = \frac{L^2}{2}(\alpha + \beta). \quad \text{(B35)}$$

In fact, by using the moment-generating function, it is possible to show that the entire process becomes Gaussian (Elston, 1999).

Within the fast kinetics approximation, the results for the average velocity are valid in general and identical with those reported above. However, the effective diffusion coefficient is only valid when the system is viewed on times scales that are long in comparison with those set by the chemical kinetics and D, and length scales that are much larger than L. In this limit, and using the technique described above, we find (Elston, 1999)

$$D_{eff} = \frac{D(p_1^{(e)}\omega_p)^2}{2} \times \frac{a(6 + a + bK' + 6a^2K'^2) - 2p_1^{(e)}\omega_p(-(3+2a) + cK' - 3a^2K'^2 + a^3K'^3)}{(a - p_1^{(e)}\omega_p(aK' - 1))^3}, \quad \text{(B36)}$$

where

$$a = \exp(-p_1^{(e)}\omega_p) - 1, \quad \text{(B37)}$$

$$b = 11 - 12\exp(-p_1^{(e)}\omega_p) + \exp(-2p_1^{(e)}\omega_p), \quad \text{(B38)}$$

$$c = -3 + \exp(-p_1^{(e)}\,\omega_p) + 2\exp(-2p_1^{(e)}\,\omega_p). \tag{B39}$$

The effective diffusion coefficient of the Brownian ratchet is found by taking the limit $\omega_p \to 0$ in the above equations. This produces

$$\lim_{\omega_p \to 0} D_{eff} = \frac{2D}{3}\frac{(1 + 6K' + 6K'^2)}{(1 + 2K')^2}. \tag{B40}$$

In the limit $K' \to 0$ ($p_1^{(e)} \to 1$), D_{eff} for the power stroke model is

$$\lim_{K' \to o} D_{eff} = D\frac{\omega_p^2\, e^{\omega_p}(1 + 4e^{\omega_p} - 5e^{2\omega_p} + 2e^{\omega_p}(2 + e^{\omega_p})\omega_p)}{2(1 - e^{\omega_p} + \omega_p e^{\omega_p})}. \tag{B41}$$

Taking the limit $\omega_p \to 0$ in Eq. B41 or $K' \to 0$ in Eq. B40 produces the result

$$\lim_{\omega_p \to 0, K' \to o} D_{eff} = \frac{2D}{3}, \tag{B42}$$

which is the effective diffusion coefficient of a perfect Brownian ratchet. Not surprisingly, for both models as $K' \to \infty$ ($p_1^{(e)} \to 0$), D_{eff} goes to D, because, in this case, there is no Hsp-70 bound to the precursor, which means the precursor is undergoing pure diffusion.

APPENDIX C: NUMERICAL METHOD

Details of the numerical algorithm have been described elsewhere (Elston and Doering, 1995; Elston and Peskin, 1998). The general procedure is to approximate the spatially continuous Markov process described by Eqs. 4 and 5 by a Markov chain. This algorithm has the advantage that it preserves the property of detailed balance for equilibrium processes. For the results presented in the manuscript, five sites along the chain were kept track of, and the sixth site was assumed to be in chemical equilibrium. The grid spacing used in the simulations was $L/20$. Each realization of the process was carried out for 25,000 time steps. In this algorithm, each time step is a random variable, so the total length of time varied for each realization. The data points shown have all been averaged over 20 realizations and the width of the error bars are four times the standard error.

APPENDIX D: THE FRACTION OF RELEASED PROTEINS

The method for measuring the mean velocity and effective diffusion coefficient relies on data for the fraction protein released from the membrane $p(t)$, or equivalently the fraction of proteins still associated with the membrane $1 - p(t)$. Either the experimental arrangement of Ungermann et al. (1996), in which the "backsliding" of DHFR fusion proteins is monitored, or the arrangement of Matlack et al. (1999), in which proteins released from the channel on the lumenal side are monitored, can be used. The only difference in these arrangements is the sign of the mean velocity v. In the backsliding experiments $v < 0$. For simplicity, we will focus on the case where $v > 0$. There are some mathematical subtleties associated with the $v < 0$ case that have been dealt with by Bulsara et al. (1996).

To compute the fraction of proteins released from the membrane, Eq. 28 must be solved subject to the boundary and initial conditions,

$$\left[\frac{\partial \rho}{\partial x} - v\rho\right]_{x=0} = 0, \tag{D1}$$

$$\rho(L_p, t) = 0, \tag{D2}$$

$$\rho(x, 0) = \delta(x - x'). \tag{D3}$$

In this case, $\rho(x, t)$ is the probability density for the precursor to have moved a distance x through the pore, L_p is the length of the precursor, and x' is its initial position. For the experiments under consideration, $x' = 0$. Eq. D1 is a reflecting boundary condition that restricts the precursor from backsliding out of the pore, and Eq. D2 is an absorbing boundary condition that models the release of the precursor into the organelle. Eq. 28 can be solved using an eigenfunction expansion, in which case, the solution is written in terms of the infinite series,

$$\rho(x, t) = \sum_{n=1}^{\infty} a_n \exp(-\lambda_n t) q_n(x). \tag{D4}$$

The eigenfunctions have the form

$$q_n(x) = \exp\left(\frac{\omega}{2}\frac{x}{L_p}\right)\sin\left[\frac{\beta_n}{L_p}(x - L_p)\right], \tag{D5}$$

where $\omega = vL_p/D$ and β_n is found from the characteristic equation,

$$-\frac{2\beta_n}{\omega} = \tan\beta_n. \tag{D6}$$

The eigenvalues are related to β_n through the relation

$$\lambda_n = \frac{D_{eff}}{L_p^2}\left(\frac{\omega^2}{4} + \beta_n^2\right), \tag{D7}$$

and the coefficients in Eq. D4 have the form

$$a_n = \frac{1}{L_p}\frac{\exp\left(-\frac{\omega}{2}\frac{x'}{L}\right)\sin\left(\frac{\beta_n}{L_p}(x' - L_p)\right)}{\frac{1}{2} - \frac{\sin(2\beta_n)}{\beta_n}}. \tag{D8}$$

The fraction of proteins that have been released is computed as follows:

$$\begin{aligned} p(t) &= 1 - \text{Probability of not being released} \\ &= 1 - \int_0^{L_p} \rho(x, t)\, dx \\ &= 1 - \sum_{n=0}^{\infty} b_n e^{-\lambda_n t}, \end{aligned} \tag{D9}$$

where b_n is given by

$$b_n = a_n\frac{2(-2e^{\omega/2}\beta_n + 2\beta_n\cos(\beta_n) + \omega\sin(\beta_n))}{\omega^2 + 4\beta^2}. \tag{D10}$$

In the case of the bacterial flagellar motor, useful information about the motor was gained by measuring the statistics of the time for the motor to move through a specified angle (Samuel and Berg, 1995). That is, first-passage time statistics were measured. In the case of protein translocation, the first-passage time corresponds to the time at which the precursor is released from the membrane. The first-passage time density $g(t)$ is related to $p(t)$, and, for completeness, we discuss first-passage time statistics here.

The probability density for the first-passage time can be computed as

$$g(t) = \frac{\mathrm{d}p(t)}{\mathrm{d}t} = \sum_{n=0}^{\infty} \lambda_n b_n e^{-\lambda_n t}, \tag{D11}$$

From which the mean and the variance in the time for the chain to move through a distance L_p can be computed,

$$\mathrm{E}[t] = \int_0^{\infty} t g(t)\, \mathrm{d}t = \sum_{n=0}^{\infty} \frac{b_n}{\lambda_n}, \tag{D12}$$

$$\begin{aligned} \mathrm{Var}[t] &= \mathrm{E}[t^2] - \mathrm{E}[t]^2 \\ &= \int_0^{\infty} t^2 g(t)\, \mathrm{d}t - \left(\int_0^{\infty} t g(t)\, \mathrm{d}t \right)^2 \\ &= 2 \sum_{n=0}^{\infty} \frac{b_n}{\lambda_n^2} - \left(\sum_{n=0}^{\infty} \frac{b_n}{\lambda_n} \right)^2. \end{aligned} \tag{D13}$$

The author thanks G. Oster for his willingness to discuss all aspects of the manuscript. The author would also like to thank T. Rapoport for sharing unpublished results and the two anonymous referees, whose critical comments vastly improved the quality of the manuscript.

REFERENCES

Bulsara, A., T. Elston, C. Doering, S. Lowen, and K. Lindenberg. 1996. Cooperative behavior in periodically driven noisy integrate-fire models of neuronal dynamics. *Phys. Rev. E.* 53:3958–3969.

Chauwin, J. F., G. Oster, and B. S. Glick. 1998. Strong precursor-interactions constrain models for mitochondrial import. *Biophys. J.* 74:1732–1743.

Elston, T. 2000. A macroscopic description of biomolecular transport. *J. Math. Biol.* DOI 10.1007/S002850000043.

Elston, T., and C. Doering. 1995. Numerical and analytical studies of nonequilibrium fluctuation-induced transport processes. *J. Stat. Phys.* 83:359–383.

Elston, T., and C. Peskin. 1998. The role of protein flexibility in molecular motor function: coupled diffusion in a tilted periodic potential. *SIAM.* 60:842–867.

Glick, B. 1995. Can Hsp70 proteins act as force-generating motors? *Cell.* 80:11–14.

Gorlich, D., and T. Rapoport. 1993. Protein translocation into proteoliposomes reconstituted from purified components of the endoplasmic reticulum membrane. *Cell.* 75:615–630.

Horst, M., A. Azem, G. Schatz, and B. Glick. 1997. What is the driving force for protein import into mitochondria? *Biochim. Biophys. Acta.* 1318:71–78.

Hwang, S., C. Watcher, and G. Schatz. 1991. Protein import into the yeast mitochondrial matrix. A new translocation intermediate between the two mitochondrial membranes. *J. Biol. Chem.* 266:21083–21089.

Lubensky, D., and D. Nelson. 1999. Driven polymer translocation through a narrow pore. *Biophys. J.* 77:1824–1838.

Matlack, K., B. Misselwitz, K. Plath, and T. Rapoport. 1999. BiP acts as a molecular ratchet during posttranslational transport of prepro-α factor across the ER membrane. *Cell.* 97:553–564.

Matlack, K., K. Plath, B. Misselwitz, and T. Rapoport. 1997. Protein transport by purified yeast complex and Kar2p without membranes. *Science.* 277:938–941.

Panzner, S., L. Dreier, E. Hartmann, S. Kostka, and T. Rapoport. 1995. Posttranslational protein transport in yeast reconstituted with a purified complex of Sec proteins and Kar2p. *Cell*. 81:561–570.

Peskin, C. P., G. M. Odell, and G. F. Oster. 1993. Cellular motions and thermal fluctuations: the Brownian ratchet. *Biophys. J.* 65:316–324.

Samuel, A. D. T., and H. C. Berg. 1995. Fluctuation analysis of the rotational speeds of the bacterial flagellar motor. *Proc. Natl. Acad. Sci. USA.* 92:3502–3506.

Schneider, H. J., J. Berthold, M. Bauer, K. Dietmeier, B. Guiard, M. Brunner, and W. Neupert. 1994. Mitochondrial Hsp70/MIM44 complex facilitates protein import. *Nature.* 371:768–774.

Schwartz, P., S. Huang, and A. Matouschek. 1999. The structure of precursor proteins during import into mitochondria. *J. Biol. Chem.* 274:12759–12764.

Simon, M. S., C. S. Peskin, and G. Oster. 1992. What drives the translocation of proteins? *Proc. Natl. Acad. Sci. USA.* 89:3770–3774.

Ungermann, C., B. Guiard, W. Neupert, and D. Cyr. 1996. The $\Delta\psi$ and Hsp70/MIM44-dependent reaction cycle driving early steps of protein import into the mitochondria. *EMBO J.* 15:734–744.

Voisine, C., E. Craig, N. Zufall, O. von Ahsen, N. Pfanner, and W. Voos. 1999. The protein import motor of mitochondria: unfolding and trapping of preproteins are distinct and separable functions of Matrix Hsp70. *Cell.* 97:565–574.

Wang, H., T. Elston, A. Mogilner, and G. Oster. 1998. Force generation in RNA polymerase. *Biophys. J.* 74:1186–1202.